Available online at www.sciencedirect.com

ScienceDirect

Ceramics International 40 (2014) 4395–4405

CERAMICS INTERNATIONAL

www.elsevier.com/locate/ceramint

# Solubility studies and thermophysical properties of uranium–neodymium mixed oxides system

R. Venkata Krishnan[a], R. Babu[a], G. Panneerselvam[a], Brij Mohan Singh[b], Abhiram Senapati[a], K. Ananthasivan[a,*], M.P. Antony[a], K. Nagarajan[a]

[a]*Fuel Chemistry Division, Indira Gandhi Centre for Atomic Research, Kalpakkam 603102, Tamil Nadu, India*
[b]*Babha Atomic Research Centre, Trombay, Mumbai 400085, India*

Received 22 April 2013; received in revised form 27 August 2013; accepted 27 August 2013
Available online 12 September 2013

**Abstract**

Uranium–neodymium mixed oxides $(U_{1-y}Nd_y)O_{2\pm x}$ ($y=0.2$–$0.85$) were prepared by citrate gel-combustion and characterized by XRD. Single phase fluorite structure was observed up to $y=0.80$. For solid solutions with $y>0.80$ additional lines pertaining to hexagonal neodymium oxide were observed. Lattice thermal expansion of these samples was investigated by using high temperature X-ray diffraction (HTXRD). The coefficients of thermal expansion for $(U_{1-y}Nd_y)O_{2\pm x}$ for $y=0.2$, 0.4, 0.6, and 0.8 in the temperature range 298–1973 K were found to be 16.46, 16.64, 16.79, and $16.89\times10^{-6}$ $K^{-1}$, respectively. Heat capacity and enthalpy increment measurements were carried out by using DSC and drop calorimetry in the temperature range 298–800 K and 800–1800 K respectively. The $C_{p,m}$ values at 298 K for $(U_{1-y}La_y)O_{2\pm x}$ ($y=0.2$, 0.4, 0.6, and 0.8) are 63.4, 64.3, 61.8, and 58.9 J $K^{-1}$ $mol^{-1}$ respectively.


*Keywords:* C. Thermal expansion; Uranium; Neodymium; Solid solution; Heat capacity

## 1. Introduction

Solid solutions of uranium–plutonium mixed oxides are used as fuels in fast reactors. During irradiation, a number of fission products are introduced into the fuel matrix which significantly alter the composition and physiochemical properties of the latter [1–3]. Further, the thermal gradient results in chemical potential gradients of fuel constituents (viz., U, Pu and fission products) leading to the transport of these materials radially and axially across the fissile column. Thus the composition of the fuel changes as a function of time and the radial position due to the thermally induced transport phenomena and the chemical interactions among the fuel constituents (including fission products). Therefore, knowledge of the chemical states of these fission products is quite relevant and useful for they significantly influence many physicochemical properties of the fuel. The extreme chemical environment can affect the mechanical as well as chemical properties of cladding and could lead to clad wastage and clad failure. All the above interactions in turn decide the fuel performance and limit the life of the fuel in the reactor. It is useful to have a good understanding of the physicochemical processes involving the formation of various compounds and their thermophysical and thermochemical properties. Among the fission products the rare earths form a sizable fraction (fission yield 50 at%) [4]. One of the major rare earth fission product elements is Nd (fission yield 20 at%) [4]. The heat capacity, enthalpy increment and thermal expansion characteristics of uranium–neodymium mixed oxides are therefore important in understanding the in-pile behavior of the fuel. In the present work, the solid solutions $(U_{1-y}Nd_y)O_{2\pm x}$ with different compositions ($y=0.2$–$0.85$) were prepared by the citrate gel-combustion route. These specimens were investigated for the extent of solid solubility of the constituent members by using X-ray diffraction (XRD). Measurements on their heat capacity were carried out by using differential scanning calorimeter (DSC) in the temperature range 298–800 K while, enthalpy increment measurements were carried out by using a high temperature drop calorimeter in the temperature range 800–1800 K. Thermal expansion characteristics

*Corresponding author. Tel.: +91 44 27480500x24069; fax: +91 44 27480065.
*E-mail addresses:* asivan@igcar.gov.in, ananthasivank@gmail.com (K. Ananthasivan).

0272-8842/$ - see front matter © 2013 Elsevier Ltd and Techna Group S.r.l. All rights reserved.
http://dx.doi.org/10.1016/j.ceramint.2013.08.111

were studied by using HTXRD in the temperature range 298–1973 K for all the single phase mixed oxides ($y=0.2$–$0.8$). The results are discussed in the paper.

## 2. Experimental

### 2.1. Sample preparation

Neodymium oxide of 99.9% purity supplied by M/s. Indian Rare Earths and nuclear grade uranium oxide supplied by NFC, Hyderabad were used for preparing the samples. These solid solutions $(U_{1-y}Nd_y)O_{2\pm x}$ ($y=0.2$–$0.85$) were prepared by citrate gel combustion syntheses. $UO_2$ was converted into $U_3O_8$ by heating in air at 873 K for 6 h. $Nd_2O_3$ was heated in air at 673 K in order to remove the adsorbed gases. Stoichiometric amounts of $U_3O_8$ and $Nd_2O_3$ were dissolved in concentrated nitric acid by heating at 353 K. The excess nitrate was removed by heating the mixture until near dryness. The nitrate salts obtained was dissolved in distilled water. The concentration of nitrate present in the solution was determined by titrametry. Citric acid was then added to this nitrate solution and clear solution was obtained. The relative amounts of the metal nitrate and citric acid were so chosen as to maintain the ratio of citric acid to nitrate ion as unity. The solution was then heated in a hot plate. Combustion of the mixture took place with a flame. The resultant fine powder was calcined at 1073 K in air for 4 h in order to remove the carbonaceous material from the sample. This powder was designated as the calcined powder. The calcined powder was compacted into pellets using a double acting hydraulic press. These sample pellets were reduced by heating in a stream of Ar+8% $H_2$ gas mixture at 873 K. Subsequently these pellets were sintered by at 1873 K for 6 h. The heating/cooling rate maintained was 250 K $min^{-1}$. Before heating the samples, the furnace was evacuated ($10^{-3}$ mbar) and filled with ultra high pure Ar+8% $H_2$ gas mixture three times. The sintered pellets were stored in an argon atmosphere glove box containing less than 20 ppm of moisture and oxygen in order to prevent oxidation of these samples.

### 2.2. Sample characterization

The concentrations of U and Nd in the sample pellet were determined by inductively coupled plasma atomic emission spectroscopy (ICP-AES), the concentrations of other metallic impurities were determined by using an inductively coupled plasma-mass spectrometer (ICP-MS) (model number ELAN 250 of M/s. Perkn Helmer, Canada) and oxygen to metal ratio (O/M) by the spectrophotometric method. The procedures for the analyses using ICP-AES, ICP-MS and spectrophotometric methods were described in our previous publications [5–7]. Structural characterization was carried out by using XRD. The XRD patterns were recorded in the range, $10^\circ < 2\theta < 80^\circ$. Peak positions and their relative intensities were computed by using a peak-fit program of the Philips X'pert Plus® software. The calibration of the diffractometer was carried out by using single crystal silicon and $\alpha$-alumina standards. The lattice parameter pertaining to the solid solution samples was estimated by considering the eight major reflections of the $CaF_2$ structure. Finally an effective high angle corrected lattice parameter at each temperature was obtained by the standard Nelson Riley extrapolation procedure.

### 2.3. Thermal expansion studies

These HTXRD studies were performed in a Philips-X'pert MPD® system, equipped with the Büehler® high vacuum heating stage. The thermal expansion characteristics of these samples were studied by using HTXRD in the temperature range 298–1973 K. Typical instrument related parameters were: operating voltage of 40 kV; current of 45 mA for the X-ray tube; scan speed 0.02 deg $s^{-1}$ with a counting time of 6 s per step in the range $20 < 2\theta < 80^\circ$. The heating stage consisted of a thin ($\sim$80 μm), resistance heated tantalum foil, on top of which the sample was placed. The temperature was measured by using a W–Re thermocouple, which was spot-welded to the bottom of the tantalum heater and controlled to an accuracy of about $\pm$1 K. The diffraction patterns of the sample holder (*Ta*) were co-recorded along with the sample for internal temperature calibration. Calibration of the diffractometer was carried out by using single crystal silicon and $\alpha$-$Al_2O_3$ standards obtained from the National Institute of Standards and Technology (NIST), USA. These diffraction studies were performed using $CuK_\alpha$ radiation in the Bragg–Brentano geometry, in steps of 100 K up to 1973 K. A heating rate of 1 K $min^{-1}$ and a holding time of 60 min at each temperature of measurement were adopted. The specimen stage was purged with high purity helium three times before the start of every experimental run and a vacuum level of about $10^{-5}$ mbar was maintained throughout the experiment. Acquisition and preliminary analysis of the data were performed by the Philips X'pert Plus® software; although independent processing of the raw data was carried out for a precise determination of the peak positions. Room temperature XRD pattern was again taken after the completion of thermal expansion measurements in order to confirm that no oxidation of the sample had taken place during the measurement.

### 2.4. Calorimetric measurements

A heat flux type differential scanning calorimeter, model number DSC821e/700 supplied by M/s. Mettler Toledo GmbH, Switzerland was used in this study. Temperature, heat flow, heat flow rate and $\tau$-lag calibrations were carried out, as explained in our previous publications [8,9]. The uncertainty in the heat capacity data measured by the DSC was estimated to be in the range of 2–3% based on our previous measurements on standard $ThO_2$ samples [10]. In order to remove the gases adsorbed on to the sample, the latter was heated to 573 K before the start of the experiment. In a typical measurement about 100–150 mg of the sample in the form of a pellet was weighed accurately and hermetically sealed into a 40 μl Al-pan. The flow rate of the purge gas (ultra high pure argon) was 50 mL $min^{-1}$. The procedures for the measurement of heat capacity by using DSC was similar to that explained in our previous publications [8,9]. The enthalpy increments of these samples in the temperature range 800–1800 K were determined by using drop a high temperature calorimeter equipped

with multi-detector (MHTC-96) supplied by M/s. SETARAM. The procedure for the measurement of enthalpy increment was as follows. The furnace was gradually heated to the desired preset temperature and argon was passed through the furnace. Once the temperature of the furnace reached the desired value, the samples were dropped from the specimen chamber. The samples maintained at the ambient temperature fell into the sample crucible maintained at the desired temperature, $T$. It took typically about 20–25 min for both the temperature and the heat flow signals to stabilize after dropping the sample. The heat flow, $Q$ (in μV) was monitored as a function of time ($t$) and the peak area $\int Qdt$ (after subtracting the baseline) associated with each drop corresponded to the respective enthalpy increment. From the resultant heat flow signals corresponding to the $\alpha$-alumina reference $Q_R$ and the sample $Q_s$, the enthalpy increments $(H_T–H_{298})_s$ of samples were computed using the known enthalpy increment values $(H_T–H_{298})_R$ pertaining to $\alpha$-alumina reference from the literature [11] and the following expression:

$$(H_T-H_{298})_S = \frac{\int Q_S dt}{\int Q_R dt}\frac{M_S}{m_S}\frac{m_R}{M_R}(H_T-H_{298})_R \quad (1)$$

where $M_R$ and $m_R$ are the molar mass and mass of the $\alpha$-alumina reference pellet and $M_S$ and $m_S$ are the molar mass and mass of the mixed oxide sample. The mean of five heat flow values pertaining to the standard and that for the sample were used to compute the enthalpy increment at a given temperature, $T$. Further, four or five such measurements were carried out at given temperature and the mean of the values of enthalpy increments obtained from these runs at a given temperature, $T$ was used for obtaining the expression for the temperature dependence of enthalpy increment through regression analysis.

## 3. Results and discussion

The results of the chemical assay of these samples carried out with the help of ICP-MS and a carbon analyzer are given in Table 1. The total concentrations of impurities were below 350 ppm. The relative concentrations of U and Nd in the solid solution determined by ICP-AES are given in Table 2. As seen in Table 2, the results of chemical assay are in good agreement ($\pm$ 1%) with the expected values. The results of O/M (M = U + Nd) measurement, lattice parameter and the phases present in these solid solutions are given in Table 3.

### 3.1. Solubility studies

The room temperature XRD patterns of $(U_{1-y}Nd_y)O_{2\pm x}$ ($y$ = 0.1–0.85) are shown in Fig. 1. As can be seen in this figure, the solid solutions $(U_{1-y}Nd_y)O_{2\pm x}$ ($y$ = 0.2–0.8) show a well-crystallized single-phase fluorite structure whereas in the XRD patterns pertaining to $y$ values greater than 0.8 the reflections pertaining to the hexagonal $Nd_2O_3$ phase (HXN)

Table 2
Relative concentrations of U and Nd determined by ICP-AES.

| Solid solutions | U (%) | Nd (%) |
|---|---|---|
| $(U_{0.8}Nd_{0.2})O_{1.95}$ | 79.8 | 20.2 |
| $(U_{0.6}Nd_{0.4})O_{1.88}$ | 60.3 | 39.7 |
| $(U_{0.4}Nd_{0.6})O_{1.73}$ | 39.9 | 60.1 |
| $(U_{0.2}Nd_{0.8})O_{1.64}$ | 20.2 | 79.8 |
| $(U_{0.18}Nd_{0.82})O_{1.61}$ | 18.1 | 81.9 |
| $(U_{0.16}Nd_{0.84})O_{1.61}$ | 16.3 | 83.7 |
| $(U_{0.15}Nd_{0.85})O_{1.61}$ | 14.9 | 85.1 |

Table 1
Concentration of impurities in (U, Nd) mixed oxides using ICP-MS.

| Elements | Solid solutions | | | |
|---|---|---|---|---|
| | $(U_{0.8}Nd_{0.2})O_{1.95}$ | $(U_{0.6}Nd_{0.4})O_{1.88}$ | $(U_{0.4}Nd_{0.6})O_{1.73}$ | $(U_{0.2}Nd_{0.8})O_{1.64}$ |
| | Concentration of impurities/ppm | | | |
| Ni | 9 | 8 | 7 | 8 |
| Zn | 3 | 2 | 2 | 4 |
| Mo | 16 | 9 | 8 | 15 |
| Ba | < 1 | < 1 | 6 | 12 |
| Al | < 1 | < 1 | 2 | 2 |
| Mg | < 1 | < 1 | < 1 | < 1 |
| Ca | < 1 | 22 | 3 | 13 |
| V | < 1 | < 1 | < 1 | < 1 |
| Cr | 9 | 7 | 16 | 6 |
| Mn | 129 | 1 | 2 | 2 |
| Fe | 56 | 45 | 16 | 90 |
| Cu | < 1 | < 1 | 2 | < 1 |
| Ce | 11 | 1 | 5 | 12 |
| La | < 1 | 6 | 35 | 4 |
| Sm | < 1 | < 1 | 1 | < 1 |
| Eu | < 1 | < 1 | < 1 | 2 |
| Gd | 9 | 28 | 31 | 32 |
| Dy | < 1 | < 1 | < 1 | < 1 |
| C | < 100 | < 100 | < 100 | < 100 |

[12] were also observed. The progressive increase in the intensity of the diffraction peaks (Fig. 1) along with the constancy of the lattice parameter (Fig. 2) values for the solid solutions substantiate the precipitation of a second phase beyond the maximum limit of the solid solubility ($y=0.8$) of $NdO_{1.5}$ in $UO_2$. From the foregoing, it can be inferred that the solubility limit of $NdO_{1.5}$ in uranium oxide lies between $y=0.80$ and 0.82. The solid solution with $y=0.82$ was sintered further at 1873 K under flowing Ar+8% $H_2$. The XRD analysis of the resultant sample also showed the presence of second phase HXN lines. Desgranges et al. [13] reported that a miscibility gap exists in the $UO_2$–$Nd_2O_3$ system [13] in the composition range spanning between compositions with $UO_2$ containing 6–40% Nd at temperatures below 1200 K. They observed a biphasic region consisting of two fluorite phases with different lattice parameters. However, our investigation shows that complete single solid solution is formed with Nd content up to 80%. To investigate the observation by Desgranges et al. [13] three different solid solutions $(U_{1-y}Nd_y)O_{2\pm x}$ (0.2, 0.3, 0.8) were prepared by citrate gel combustion synthesis, calcined at 773 K in air and reduced under flowing $H_2$ at 773 K for 8 h and the reduced powders were annealed under flowing Ar+8% $H_2$ at 1073 K for 48 h. The XRD patterns of solid solutions $(U_{1-y}Nd_y)O_{2\pm x}$ (0.2, 0.3, 0.8) (Fig. 3) show the presence of only single fluorite phase. To further confirm the solubility limit of Nd in $UO_2$, $(U_{1-y}Nd_y)O_{2\pm x}$ ($y=0.8$) sample was analyzed by transmission electron microscopy (Make: LIBRA 200 FE TEM with top entry goniometer). The reduced sample powders were suspended in isopropanol and deagglomerated by sonication by using ultrasonic bath. The drop of this suspension was placed on a copper grid coated with holey carbon film. The selected area electron diffraction (SAED) of the sample is shown in Fig. 4. The results of SAED did not confirm the existence of second phase in the solid solution. We could not comment on the observation by Desgranges et al. [13] as the stoichiometries in oxygen of their sample were not measured.

To confirm that $(U_{1-y}Nd_y)O_{2\pm x}$ ($y=0.2$, 0.4, 0.6, 0.8) solid solutions are not in meta-stable state, the samples were annealed at 773 K for 48 h and 1073 K for 48 h. The XRD patterns of the samples annealed at 773 and 1073 K are shown in Figs. 5 and 6 respectively. It is evident from the figure that only single phase fluorite solid solution is formed and they are equilibrium state solid solution. In view of the above it is reasonable to conclude that the solid solubility of $Nd_2O_3$

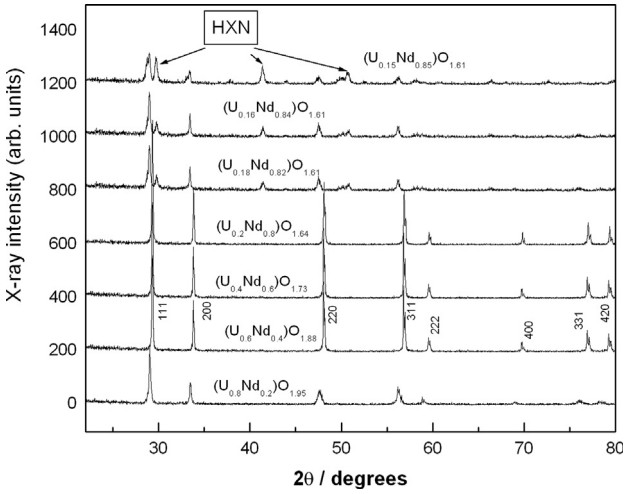


Fig. 1. Room temperature XRD patterns of $(U_{1-y}Nd_y)O_{2\pm x}$.

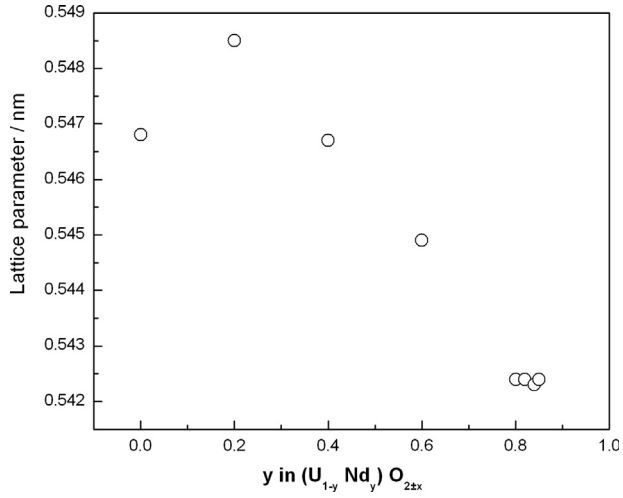


Fig. 2. Lattice parameter of $(U_{1-y}Nd_y)O_{2\pm x}$ as a function of Nd content.

Table 3
X-ray and chemical analysis of $(U_{1-y}Nd_y)O_{2\pm x}$.

| Compound | O/U | O/M | Lattice parameter (fluorite phase) (nm) | Phases present |
|---|---|---|---|---|
| $UO_{2.00}$ | 2.00 | 2.00 | 0.5468 | FCC |
| $Nd_2O_3$ | 0 | 1.5 | $a=0.38297$<br>$c=0.59987$ | HXN |
| $(U_{0.8}Nd_{0.2})$ oxide | 2.063 | 1.95 | 0.5485 | FCC |
| $(U_{0.6}Nd_{0.4})$ oxide | 2.133 | 1.88 | 0.5467 | FCC |
| $(U_{0.4}Nd_{0.6})$ oxide | 2.075 | 1.73 | 0.5449 | FCC |
| $(U_{0.2}Nd_{0.8})$ oxide | 2.200 | 1.64 | 0.5424 | FCC |
| $(U_{0.18}Nd_{0.82})$ oxide | 2.278 | 1.64 | 0.5424 | FCC+HXN |
| $(U_{0.16}Nd_{0.84})$ oxide | 2.313 | 1.63 | 0.5423 | FCC+HXN |
| $(U_{0.15}Nd_{0.85})$ oxide | 2.367 | 1.63 | 0.5424 | FCC+HXN |

(FCC: face centered cubic solid solution phase; HXN: hexagonal neodymium oxide phase).

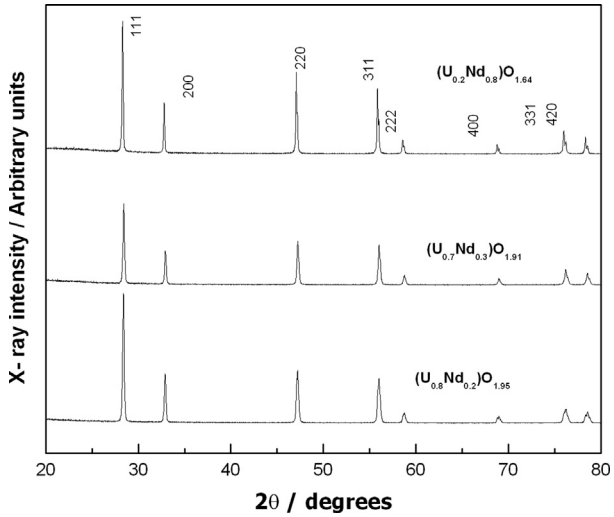


Fig. 3. Room temperature XRD patterns of $(U_{1-y}Nd_y)O_{2\pm x}$ (0.2, 0.3, 0.8) annealed at 1073 K.

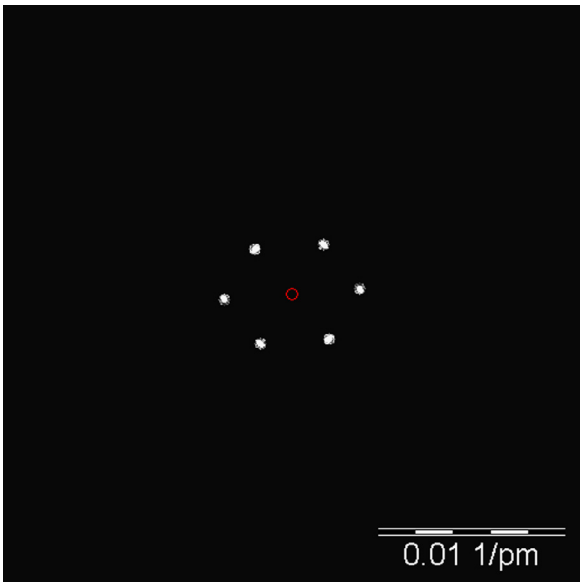


Fig. 4. SAED of $(U_{1-y}Nd_y)O_{2\pm x}$ ($y=0.8$) corresponding to a fluorite crystallite.

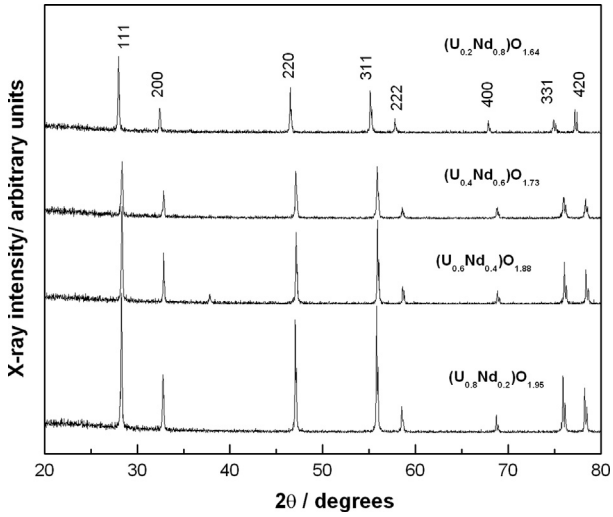


Fig. 5. Room temperature XRD patterns of sintered $(U_{1-y}Nd_y)O_{2\pm x}$ (0.2, 0.4, 0.6, 0.8) annealed at 773 K.

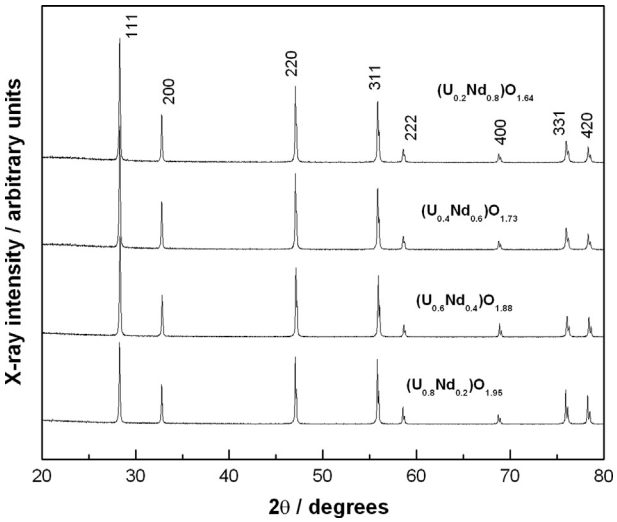


Fig. 6. Room temperature XRD patterns of sintered $(U_{1-y}Nd_y)O_{2\pm x}$ (0.2, 0.4, 0.6, 0.8) annealed at 1073 K.

in $UO_2$ is as high as 80 mol%. The results of the solubility studies are in good agreement with that reported by Kleykamp (81 mol%) [14].

As seen in Fig. 2, the lattice parameters increase with $y$ up to $y=0.2$ and decrease monotonically from $y=0.2$ to 0.8. The change in the lattice parameter of $(U_{1-y}Nd_y)O_{2\pm x}$ as a function of y are due to three factors namely (i) ionic size of the dopant, (ii) doping of cation with lower valency ($Nd^{3+}$) decreases the average ionic radii of uranium ion due to oxidation of $U^{4+}$ to $U^{5+}$ and $U^{6+}$ and (iii) with an increase in the Nd content the O/M ratio of the solid solution also decreases (Table 1) which in turn results in the creation of vacancies in the anionic sublattice. These oxide ion vacancies would also contribute to the decrease in the lattice parameter. The ionic radii of $Nd^{3+}$, $U^{4+}$, $U^{5+}$ and $U^{6+}$ with eightfold coordination are 0.1109, 0.1000, 0.088, and 0.086 nm [15] respectively. When $y$ is increased from 0 to 0.2 in $(U_{1-y}Nd_y)O_{2\pm x}$, the factor namely the doping of cation ($Nd^{3+}$) of higher ionic size predominates. However, for solid solutions with $y=0.4$ to 0.8 the factors namely oxidation of $U^{4+}$ and creation of oxygen ion vacancies predominates.

The scanning electron micrograph (SEM) of $(U_{1-y}Nd_y)O_{2\pm x}$ for $y=0.2$, 0.4, 0.6, 0.8, 0.82, 0.84 and 0.85 are shown in Figs. 7–13 correspondingly. As can be seen in these figures the solid solutions with $y$ values up to 0.8 have uniform grain size in the range of 5–10 μm with well-defined grain boundaries whereas, the solid solutions having $y$ value $>0.8$ (0.82, 0.84 and 0.85) have flaky shaped particles whose grains are not properly formed. This may be attributed to the precipitation of second phase hexagonal $Nd_2O_3$ (HXN) which are uniformly distributed throughout the matrix of the major phase. The observation is in good agreement with the investigation by XRD, which shows the precipitation of second phase HXN for the solid solution with $y>0.8$.

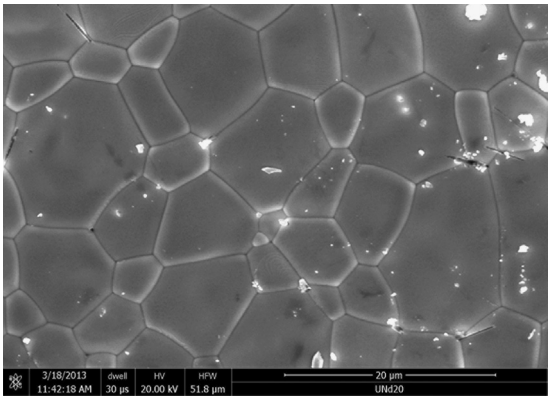


Fig. 7. SEM micrograph of $(U_{0.8}Nd_{0.2})O_{1.95}$.

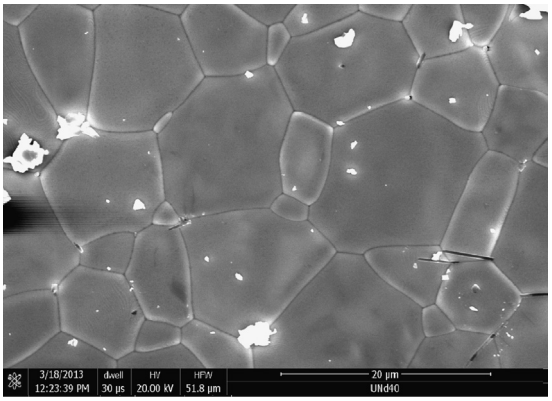


Fig. 8. SEM micrograph of $(U_{0.6}Nd_{0.4})O_{1.88}$.

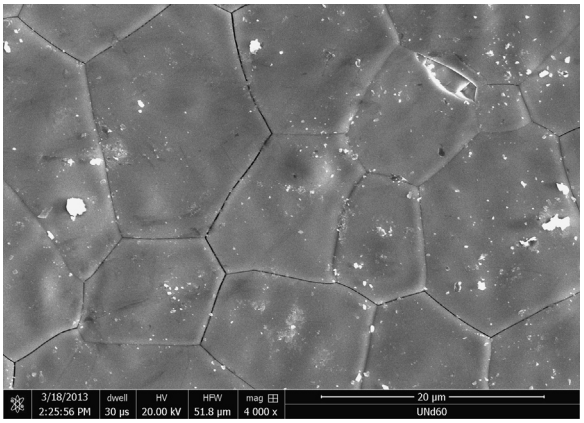


Fig. 9. SEM micrograph of $(U_{0.4}Nd_{0.6})O_{1.73}$.

### 3.2. Thermal expansion studies

The temperature dependence of the measured values of the lattice parameters of $(U_{1-y}Nd_y)O_{2\pm x}$ ($y$=0.2, 0.4, 0.6 and 0.8) in the temperature range 298–1973 K is shown in Fig. 14 and these values are listed in Table 4 as well. Least square regression analysis of these samples yielded second order polynomials represented by Eqs. (2)–(5) (298–1973 K).

$$a(\text{nm})[(U_{0.8}Nd_{0.2})O_{1.95}] = 0.5485 + 3.9517 \times 10^{-6}(T–298) + 1.5171 \times 10^{-9}(T–298)^2 \quad (2)$$

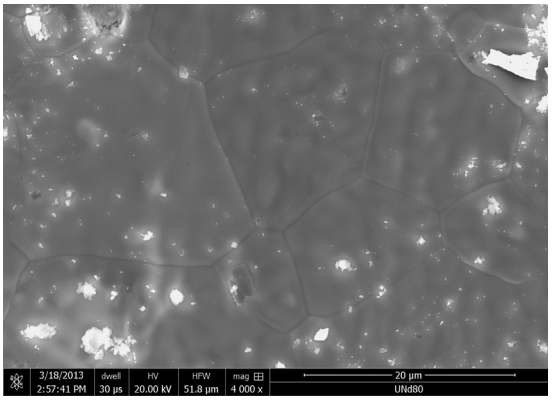


Fig. 10. SEM micrograph of $(U_{0.2}Nd_{0.8})O_{1.64}$.

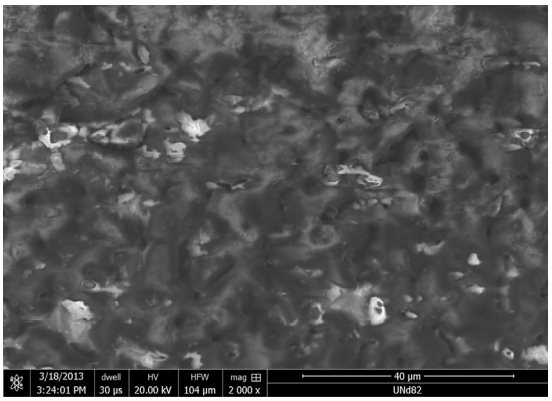


Fig. 11. SEM micrograph of $(U_{0.18}Nd_{0.82})O_{1.61}$.

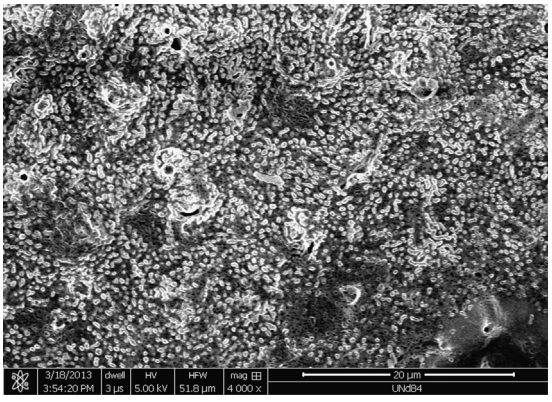


Fig. 12. SEM micrograph of $(U_{0.16}Nd_{0.84})O_{1.61}$.

$$a(\text{nm})[(U_{0.6}Nd_{0.4})O_{1.88}] = 0.5467 + 3.5693 \times 10^{-6}(T–298) + 1.6462 \times 10^{-9}(T–298)^2 \quad (3)$$

$$a(\text{nm})[(U_{0.4}Nd_{0.6})O_{1.73}] = 0.5449 + 3.3292 \times 10^{-6}(T–298) + 1.725 \times 10^{-9}(T–298)^2 \quad (4)$$

$$a(\text{nm})[(U_{0.2}Nd_{0.8})O_{1.64}] = 0.5424 + 3.1288 \times 10^{-6}(T–298) + 1.7733 \times 10^{-9}(T–298)^2 \quad (5)$$

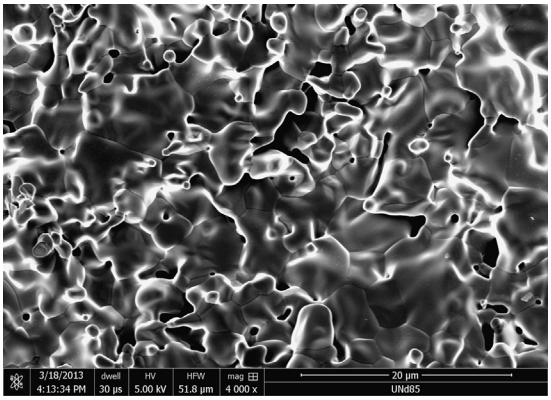


Fig. 13. SEM micrograph of $(U_{0.15}Nd_{0.85})O_{1.61}$.

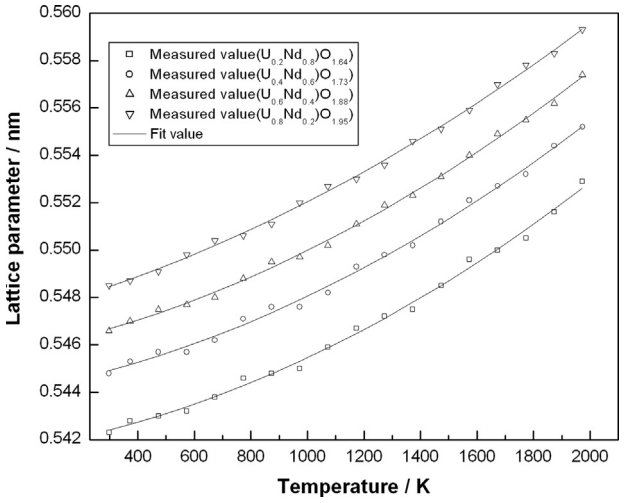


Fig. 14. Change in the lattice parameter of $(U_{1-y}Nd_y)O_{2\pm x}$ as a function of temperature.

From these expressions the values of the mean coefficient of linear thermal expansion ($\alpha_m$) were computed by using the expression given below. They are presented in Table 4.

$$\alpha_m = 1/a_{298}(da/dT) \quad (6)$$

The mean percentage of thermal expansion of pertaining to the solid solution $(U_{1-y}Nd_y)O_{2\pm x}$ ($y=0.2$, 0.4, 0.6 and 0.8) solid solutions were computed from the expressions 2-5. They are depicted in Table 4 and are shown in Fig. 15.

### 3.3. Calorimetric measurements

The measured values of the enthalpy increments in the temperature range 800–1800 K were fitted into a four term polynomial function represented below (by least squares regression analysis)

$$H_T - H_{298}/\text{J mol}^{-1} = AT + B\times 10^{-3}T^2 + C\times 10^{5}T^{-1} + D\times 10^{4} \quad (7)$$

The constraints used for this fit were (i) $H_T - H_{298}=0$ at 298 K and (ii) the temperature derivative of the function at 298 K is equal to $C_{p,\ 298}$ measured by DSC measurements. The coefficients of the polynomials pertaining to the solid solutions $(U_{1-y}Nd_y)O_{2\pm x}$ ($y=0.2$, 0.4, 0.6, 0.8) are presented in Table 5.

The values of the heat capacity by DSC and those computed from the enthalpy increment by drop calorimetry measurements were fitted into a polynomial through a least squares regression analysis. The expressions corresponding to the solid solutions $(U_{1-y}Nd_y)O_{2\pm x}$ ($y=0.2$, 0.4, 0.6, 0.8) are presented in Table 6. From the heat capacity data, the enthalpy, entropy and Gibbs energy functions were computed. These are presented in Tables 7–10. The value of $S_{298}$ data pertaining to $(U_{1-y}Nd_y)O_{2\pm x}$, required for the computation of the $S_T^0$ were estimated by

Table 4
Lattice parameters of $(U_{1-y}Nd_y)O_{2\pm x}$ solid solutions as a function of temperature.

| $T$ (K) | $(U_{0.8}Nd_{0.2})O_{1.95}$ | | $(U_{0.6}Nd_{0.4})O_{1.88}$ | | $(U_{0.4}Nd_{0.6})O_{1.73}$ | | $(U_{0.2}Nd_{0.8})O_{1.64}$ | |
|---|---|---|---|---|---|---|---|---|
| | $a$ (nm) | $\alpha_m$ ($10^6$ K$^{-1}$) | $a$ (nm) | $\alpha_m$ ($10^6$ K$^{-1}$) | $a$ (nm) | $\alpha_m$ ($10^6$ K$^{-1}$) | $a$ (nm) | $\alpha_m$ ($10^6$ K$^{-1}$) |
| 298 | 0.5485 | 7.22 | 0.5467 | 6.56 | 0.5449 | 6.04 | 0.5424 | 5.62 |
| 373 | 0.5488 | 7.64 | 0.5470 | 7.01 | 0.5452 | 6.52 | 0.5427 | 6.12 |
| 473 | 0.5492 | 8.19 | 0.5474 | 7.61 | 0.5455 | 7.17 | 0.5430 | 6.80 |
| 573 | 0.5497 | 8.74 | 0.5478 | 8.21 | 0.5459 | 7.81 | 0.5434 | 7.47 |
| 673 | 0.5502 | 9.29 | 0.5483 | 8.82 | 0.5464 | 8.45 | 0.5438 | 8.14 |
| 773 | 0.5507 | 9.84 | 0.5488 | 9.42 | 0.5469 | 9.09 | 0.5443 | 8.82 |
| 873 | 0.5513 | 10.40 | 0.5493 | 10.02 | 0.5474 | 9.73 | 0.5448 | 9.49 |
| 973 | 0.5519 | 10.95 | 0.5499 | 10.62 | 0.5479 | 10.37 | 0.5453 | 10.16 |
| 1073 | 0.5525 | 11.50 | 0.5504 | 11.22 | 0.5485 | 11.02 | 0.5459 | 10.83 |
| 1173 | 0.5531 | 12.05 | 0.5511 | 11.83 | 0.5491 | 11.66 | 0.5465 | 11.51 |
| 1273 | 0.5538 | 12.60 | 0.5517 | 12.43 | 0.5498 | 12.30 | 0.5471 | 12.18 |
| 1373 | 0.5545 | 13.15 | 0.5524 | 13.03 | 0.5505 | 12.94 | 0.5478 | 12.85 |
| 1473 | 0.5552 | 13.71 | 0.5532 | 13.63 | 0.5512 | 13.58 | 0.5485 | 13.52 |
| 1573 | 0.5560 | 14.26 | 0.5539 | 14.24 | 0.5520 | 14.22 | 0.5493 | 14.20 |
| 1673 | 0.5568 | 14.81 | 0.5547 | 14.84 | 0.5527 | 14.86 | 0.5501 | 14.87 |
| 1773 | 0.5576 | 15.36 | 0.5556 | 15.44 | 0.5536 | 15.51 | 0.5509 | 15.54 |
| 1873 | 0.5585 | 15.91 | 0.5564 | 16.04 | 0.5544 | 16.15 | 0.5517 | 16.21 |
| 1973 | 0.5594 | 16.46 | 0.5573 | 16.64 | 0.5553 | 16.79 | 0.5526 | 16.89 |

using Neumann–Kopp's approximation from the values of $S^0_{298}$ values of pure $Nd_2O_3$ [15] and $UO_2$ [16].

The combined fit of the heat capacity data obtained from the DSC and drop calorimetric experiments is shown in Fig. 16. As seen in this figure, considerable anomalous increase in the heat capacity is observed with onset temperatures in the range 1000–1200 K for $(U_{1-y}Nd_y)O_{2\pm x}$ ($y$=0.2, 0.4, 0.6, 0.8). Such anomalous increase in the heat capacity is usually observed when $UO_2$ is doped with an aliovalent cation ($Nd^{3+}$ in this case) [6,9,17–23]. This phenomenon could be attributed to the predominant contribution from Frenkel pair oxygen defects. A similar trend was observed in our previous studies on the measurement of heat capacity of $(U_{1-y}Gd_y)O_{2\pm x}$ [6] and $(U_{1-y}La_y)O_{2\pm x}$ [9]. An estimate of the temperature dependence of the heat capacity pertaining to the solid solutions $(U_{1-y}Nd_y)O_{2\pm x}$ ($y$=0.2, 0.4, 0.6, 0.8) over the temperature range 298–1800 K was obtained by extrapolating the expression derived through the least square regression analysis of the data in the temperature range 298–900 K. This is hence forth termed as baseline heat capacity. The baseline (298–900 K) and the combined experimentally determined temperature dependence of heat capacity data in the temperature range 298–1800 K were fitted to the following polynomials by least squares regression analysis, respectively,

$$C_p(\text{Baseline}) = A + BT + CT^{-2} \quad (8)$$

$$C_p(\text{Experimental}) = A + BT + CT^{-2} + DT^2 \quad (9)$$

The difference between these values of the heat capacity is termed as the excess heat capacity ($\Delta C_p$) [6,9]. The temperature dependence of the excess heat capacity is shown in Fig. 17. It is evident from the figure that the onset temperature of heat capacity anomaly is in the range of 900–1100 K for all the solid solutions $(U_{1-y}Nd_y)O_{2\pm x}$. In our earlier publications [6,9] on the heat capacity of $(U_{1-y}Gd_y)O_{2\pm x}$ and $(U_{1-y}La_y)O_{2\pm x}$, it was found that the onset temperature of heat capacity anomaly is in the range of 500–600 K and 1000–1200 K respectively. The difference in the onset temperature of heat capacity anomaly was attributed to the difference in the enthalpy for the formation of defects [6,9,17–24]. If $H_d$ is the enthalpy of defect formation, the number of defects $n_d$ at any temperature $T$ is given by

$$n_d = n_0 \exp(-H_d/kT) \quad (10)$$

And the excess heat capacity ($\Delta C_p$) is given by,

$$\Delta C_p = d/dT(n_d H_d) = (n_0 E_d^2/kT^2)\exp(-H_d/kT) \quad (11)$$

Therefore, the plot of $\ln(T^2\Delta C_p)$ against $1/T$ is a straight line with a slope of $-H_d/k$. The plot of $\ln(T^2\Delta C_p)$ against $1/T$ for $(U_{1-y}Nd_y)O_{2\pm x}$ ($y$=0.2, 0.4, 0.6, 0.8) is shown in Fig. 18 and the enthalpy of defect formation computed from the slopes are between 1.05 and 1.07 eV whereas, the enthalpy of defect

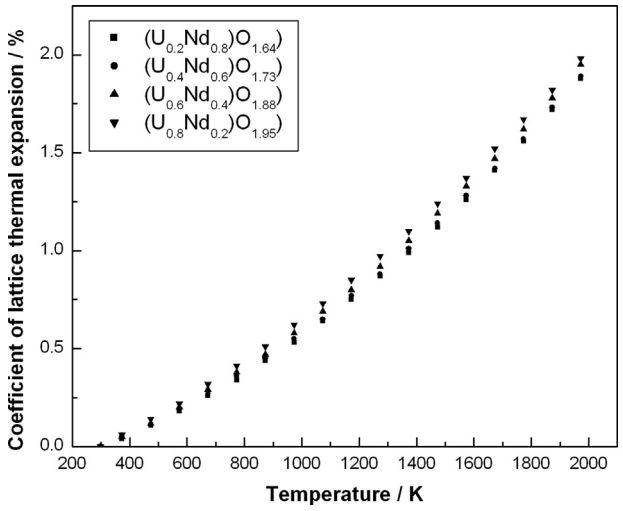


Fig. 15. Thermal expansion characteristics of $(U_{1-y}Nd_y)O_{2\pm x}$.

Table 5
Coefficients of the expression obtained by least squares regression analysis of the temperature dependence of the enthalpies obtained by drop calorimetry ($800 \le T/K \le 1800$).

| Coefficients | $(U_{0.8}Nd_{0.2})O_{1.95}$ | $(U_{0.6}Nd_{0.4})O_{1.88}$ | $(U_{0.4}Nd_{0.6})O_{1.73}$ | $(U_{0.2}Nd_{0.8})O_{1.64}$ |
|---|---|---|---|---|
| $A$ | 77.81 | 69.01 | 68.16 | 68.50 |
| $B$ | 1.859 | 3.714 | 2.846 | 1.616 |
| $C$ | 13.4035 | 6.8215 | 8.6122 | 9.2436 |
| $D$ | −2.7859 | −2.3193 | −2.3463 | −2.3665 |
| Standard error/J mol$^{-1}$ | 609 | 761 | 755 | 949 |

Expression ($H_T - H_{298}$/J mol$^{-1}$ $= AT + B\times10^{-3}T^2 + C\times10^5T^{-1} + D\times10^4$).

Table 6
Expressions obtained by least square regression analysis of the heat capacity values from DSC and drop calorimetry measurements ($298 \le T/K \le 1800$).

| S. no | Compound | Fit equation (J K$^{-1}$ mol$^{-1}$) | Standard error J K$^{-1}$ mol$^{-1}$ |
|---|---|---|---|
| 1 | $(U_{0.8}Nd_{0.2})O_{1.95}$ | $85.49 - 5.89\times10^{-3}T - 1.828603\times10^6T^{-2} - 3.0328\times10^6T^{-2}$ | 0.35 |
| 2 | $(U_{0.6}Nd_{0.4})O_{1.88}$ | $78.83 - 7.29\times10^{-3}T - 1.134468\times10^6T^{-2} + 5.3802\times10^6T^{-2}$ | 0.69 |
| 3 | $(U_{0.4}Nd_{0.6})O_{1.73}$ | $75.76 - 5.86\times10^{-3}T - 1.179640\times10^6T^{-2} + 4.2573\times10^6T^{-2}$ | 0.92 |
| 4 | $(U_{0.2}Nd_{0.8})O_{1.64}$ | $73.10 - 3.24\times10^{-3}T - 1.193696\times10^6T^{-2} + 2.2558\times10^6T^{-2}$ | 0.52 |

Table 7
Thermodynamic functions pertaining to $(U_{0.8}Nd_{0.2})O_{1.95}$.

| $T$ (K) | $C_{p,m}$/J K$^{-1}$ mol$^{-1}$ | | $H_T-H_{298}$/J mol$^{-1}$ | | $S_T$ | $G_T-H_{298}/T$ |
|---|---|---|---|---|---|---|
| | Measured | Fit | Measured | Fit | (J K$^{-1}$ mol$^{-1}$) | (J K$^{-1}$ mol$^{-1}$) |
| 298 | 63.4 | 63.4 | | 0 | 90.7 | −90.7 |
| 300 | 63.7 | 63.7 | | 127 | 91.2 | −90.7 |
| 400 | 71.4 | 72.2 | | 6984 | 110.8 | −93.4 |
| 500 | 75.4 | 76.0 | | 14415 | 127.4 | −98.6 |
| 600 | 78.1 | 78.0 | | 22123 | 141.4 | −104.6 |
| 700 | 80.1 | 79.1 | | 29982 | 153.5 | −110.7 |
| 800 | 80.6 | 79.9 | 37253 | 37934 | 164.2 | −116.7 |
| 900 | | 80.4 | 45164 | 45948 | 173.6 | −122.5 |
| 1000 | | 80.8 | 53149 | 54009 | 182.1 | −128.1 |
| 1100 | | 81.2 | 61199 | 62108 | 189.8 | −133.4 |
| 1200 | | 81.5 | 69306 | 70242 | 196.9 | −138.4 |
| 1300 | | 81.9 | 77465 | 78412 | 203.4 | −143.1 |
| 1400 | | 82.3 | 85675 | 86619 | 209.5 | −147.6 |
| 1500 | | 82.7 | 93931 | 94865 | 215.2 | −152.0 |
| 1600 | | 83.1 | 102232 | 103154 | 220.6 | −156.1 |
| 1700 | | 83.6 | 110577 | 111490 | 225.6 | −160.0 |
| 1800 | | 84.2 | 118965 | 119878 | 230.4 | −163.8 |

Table 8
Thermodynamic functions pertaining to $(U_{0.6}Nd_{0.4})O_{1.88}$.

| $T$ (K) | $C_{p,m}$/J K$^{-1}$ mol$^{-1}$ | | $H_T-H_{298}$/J mol$^{-1}$ | | $S_T$ | $G_T-H_{298}/T$ |
|---|---|---|---|---|---|---|
| | Measured | Fit | Measured | Fit | (J K$^{-1}$ mol$^{-1}$) | (J K$^{-1}$ mol$^{-1}$) |
| 298 | 64.3 | 64.4 | | 0 | 85.4 | −85.4 |
| 300 | 65.3 | 64.5 | | 129 | 85.8 | −85.4 |
| 400 | 70.5 | 69.7 | | 6877 | 105.2 | −88.0 |
| 500 | 72.3 | 72.0 | | 13974 | 121.0 | −93.1 |
| 600 | 73.5 | 73.2 | | 21241 | 134.3 | −98.9 |
| 700 | 74.2 | 74.0 | | 28607 | 145.6 | −104.7 |
| 800 | 75.3 | 74.7 | 35244 | 36043 | 155.5 | −110.5 |
| 900 | | 75.2 | 42681 | 43538 | 164.4 | −116.0 |
| 1000 | | 75.8 | 50212 | 51088 | 172.3 | −121.2 |
| 1100 | | 76.4 | 57831 | 58695 | 179.6 | −126.2 |
| 1200 | | 77.0 | 65534 | 66366 | 186.2 | −130.9 |
| 1300 | | 77.8 | 73320 | 74105 | 192.4 | −135.4 |
| 1400 | | 78.6 | 81186 | 81922 | 198.2 | −139.7 |
| 1500 | | 79.5 | 89132 | 89825 | 203.7 | −143.8 |
| 1600 | | 80.5 | 97155 | 97823 | 208.8 | −147.7 |
| 1700 | | 81.6 | 105257 | 105926 | 213.8 | −151.4 |
| 1800 | | 82.8 | 113435 | 114144 | 218.5 | −155.0 |

Table 9
Thermodynamic functions pertaining to $(U_{0.4}Nd_{0.6})O_{1.73}$.

| $T$ (K) | $C_{p,m}$/J K$^{-1}$ mol$^{-1}$ | | $H_T-H_{298}$/J mol$^{-1}$ | | $S_T$ | $G_T-H_{298}/T$ |
|---|---|---|---|---|---|---|
| | Measured | Fit | Measured | Fit | (J K$^{-1}$ mol$^{-1}$) | (J K$^{-1}$ mol$^{-1}$) |
| 298 | 61.8 | 61.1 | | 0 | 81.5 | −81.5 |
| 300 | 62.1 | 61.3 | | 123 | 81.9 | −81.5 |
| 400 | 68.4 | 66.7 | | 6564 | 100.4 | −84.0 |
| 500 | 70.3 | 69.2 | | 13373 | 115.6 | −88.8 |
| 600 | 71.1 | 70.5 | | 20363 | 128.3 | −94.3 |
| 700 | 72.5 | 71.3 | | 27458 | 139.2 | −100.0 |
| 800 | 73.3 | 72.0 | 33963 | 34625 | 148.8 | −105.5 |
| 900 | | 72.5 | 41144 | 41848 | 157.3 | −110.8 |

**Table 9** (*continued*)

| $T$ (K) | $C_{p,m}$/J K$^{-1}$ mol$^{-1}$ | | $H_T-H_{298}$/J mol$^{-1}$ | | $S_T$ | $G_T-H_{298}/T$ |
|---|---|---|---|---|---|---|
| | Measured | Fit | Measured | Fit | (J K$^{-1}$ mol$^{-1}$) | (J K$^{-1}$ mol$^{-1}$) |
| 1000 | | 73.0 | 48405 | 49121 | 164.9 | −115.8 |
| 1100 | | 73.5 | 55740 | 56446 | 171.9 | −120.6 |
| 1200 | | 74.0 | 63146 | 63823 | 178.3 | −125.1 |
| 1300 | | 74.6 | 70618 | 71257 | 184.3 | −129.5 |
| 1400 | | 75.3 | 78156 | 78755 | 189.8 | −133.6 |
| 1500 | | 76.0 | 85756 | 86322 | 195.0 | −137.5 |
| 1600 | | 76.8 | 93419 | 93965 | 200.0 | −141.2 |
| 1700 | | 77.7 | 101142 | 101691 | 204.7 | −144.8 |
| 1800 | | 78.6 | 108927 | 109509 | 209.1 | −148.3 |

Table 10
Thermodynamic functions pertaining to ($U_{0.2}$ $Nd_{0.8}$) $O_{1.64}$

| $T$ (K) | $C_{p,m}$/J K$^{-1}$ mol$^{-1}$ | | $H_T-H_{298}$/J mol$^{-1}$ | | $S_T$ | $G_T-H_{298}/T$ |
|---|---|---|---|---|---|---|
| | Measured | Fit | Measured | Fit | (J K$^{-1}$ mol$^{-1}$) | (J K$^{-1}$ mol$^{-1}$) |
| 298 | 58.9 | 58.9 | | 0 | 79.0 | −79.0 |
| 300 | 59.1 | 59.1 | | 118 | 79.4 | −79.0 |
| 400 | 64.2 | 64.7 | | 6348 | 97.3 | −81.5 |
| 500 | 67.5 | 67.3 | | 12961 | 112.1 | −86.2 |
| 600 | 68.5 | 68.7 | | 19763 | 124.5 | −91.5 |
| 700 | 69.8 | 69.5 | | 26674 | 135.1 | −97.0 |
| 800 | 70.6 | 70.1 | 33320 | 33655 | 144.5 | −102.4 |
| 900 | | 70.5 | 40316 | 40687 | 152.7 | −107.5 |
| 1000 | | 70.9 | 47370 | 47760 | 160.2 | −112.4 |
| 1100 | | 71.3 | 54474 | 54870 | 167.0 | −117.1 |
| 1200 | | 71.6 | 61626 | 62015 | 173.2 | −121.5 |
| 1300 | | 72.0 | 68820 | 69196 | 179.0 | −125.7 |
| 1400 | | 72.4 | 76055 | 76414 | 184.3 | −129.7 |
| 1500 | | 72.8 | 83329 | 83671 | 189.3 | −133.5 |
| 1600 | | 73.2 | 90641 | 90971 | 194.0 | −137.2 |
| 1700 | | 73.7 | 97990 | 98317 | 198.5 | −140.7 |
| 1800 | | 74.2 | 105375 | 105711 | 202.7 | −144.0 |

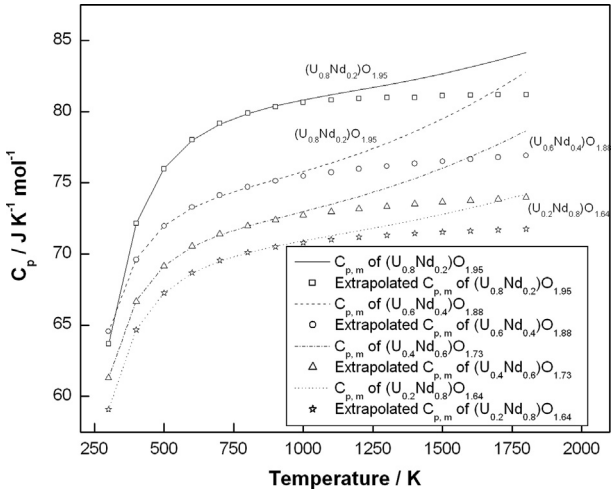


Fig. 16. Heat capacity data of $(U_{1-y}Nd_y)O_{2\pm x}$ from DSC and drop calorimetry.

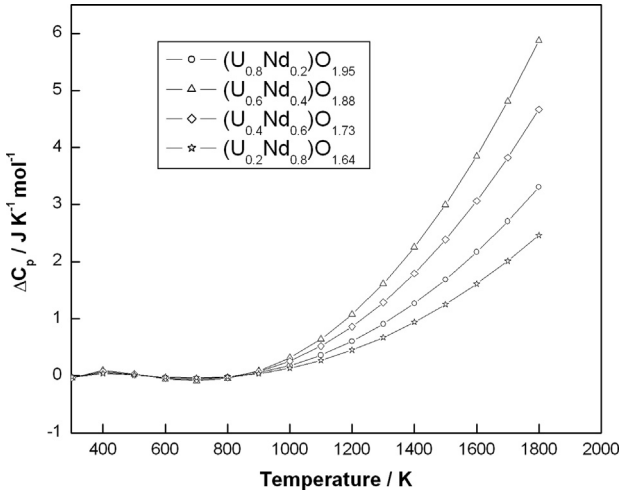


Fig. 17. Difference between the baseline and measured heat capacity data ($\Delta C_p$) vs $T$ of $(U_{1-y}Nd_y)O_{2\pm x}$.

formation for $(U_{1-y}Gd_y)O_{2\pm x}$ and $(U_{1-y}La_y)O_{2\pm x}$ [6,7] were in the range of 0.57–0.81 eV and 1.31–1.33 eV respectively. The onset temperature of heat capacity anomaly lies between that for $(U_{1-y}Gd_y)O_{2\pm x}$ and $(U_{1-y}La_y)O_{2\pm x}$. This is because the enthalpy of defect formation for $(U_{1-y}Nd_y)O_{2\pm x}$ is in the range between that of $(U_{1-y}Gd_y)O_{2\pm x}$ and $(U_{1-y}La_y)O_{2\pm x}$.

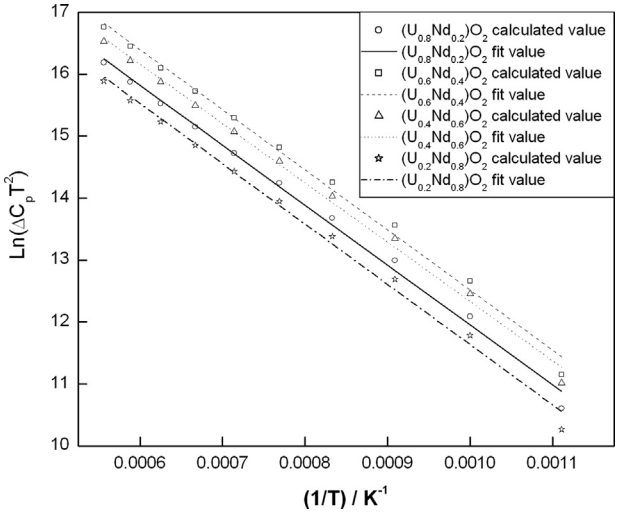


Fig. 18. Plot of $\ln(T^2\Delta C_p)$ vs $1/T$ in the temperature range 900–1800.

## 4. Conclusions

The solid solubility of $NdO_{1.5}$ in $UO_2$ is in the range of 80–82%. The miscibility gap reported in the literature in $NdO_{1.5}$–$UO_2$ system was not observed in the present investigation. Heat capacity, enthalpy increment and thermal expansion measurements of $(U_{1-y}Nd_y)O_{2\pm x}$ ($y$=0.2, 0.4, 0.6, 0.8) were carried out in the temperature range 298–800 K, 800–1800 K and 298–1973 K respectively. The heat capacity data as well as the data on the lattice thermal expansion on the system U–Nd–O are being reported for the first time over the entire composition range. An anomalous increase in the heat capacity is observed in all these solid solutions. This phenomenon is attributed to the formation of Frenkel defect pair of oxygen. From the excess heat capacity data, the enthalpy for the formation of defect was estimated to be in the range of 1.05–1.07 eV. In our heat capacity measurements on $(U_{1-y}Gd_y)O_{2\pm x}$ and $(U_{1-y}La_y)O_{2\pm x}$ [6,9] it was observed that the onset temperature of the anomalous variation in the heat capacity anomaly increases with increase in the enthalpy of defect formation. These observations suggest that the temperature of onset of the anomalous increase in heat capacity is directly correlated with the enthalpy associated with the formation of Frenkel defect pairs in the $UO_2$ lattice.

## References

[1] D.R. Olander, Fundamental Aspects of Nulcear Reactor Fuel Elements, Springfield, Virgina, 1985.
[2] H.J. Matzke, Science of Advanced LMFBR Fuels, Amsterdam, North Holland, 1986.
[3] M. Lammer, Compilation and evaluation of fission yield nuclear data, IAEA TECDOC-1168, 2000.
[4] E.A.C. Crouch, Report-AERE-R-6056, 1969.
[5] R. Venkata Krishnan, K. Nagarajan, Heat capacity measurements on uranium-cerium mixed oxides by differential scanning calorimetry, Thermochimica Acta 440 (2006) 141–145.
[6] R. Venkata Krishnan, G. Panneerselvam, P. Manikandan, M.P. Antony, K. Nagarajan, Heat capacity and thermal expansion of uranium-gadolinium mixed oxides, Journal of Nuclear and Radiochemical Sciences 10 (1) (2009) 19–26.
[7] R. Venkata Krishnan, G. Pannerselvam, M.P. Antony, K. Nagarajan, Solubility studies and thermal expansion coefficients of uranium–lanthanum mixed oxides, Journal of Nuclear Materials 403 (2010) 25–31.
[8] R. Venkata Krishnan, K. Nagarajan, Thermochimica Acta 440 (2006) 141–145.
[9] R. Venkata Krishnan, V.K. Mittal, R. Babu, A. Senapati, S. Bera, K. Nagarajan, Heat capacity measurements and XPS studies on uranium–lanthanum mixed oxides, Journal of Alloys and Compounds 509 (2011) 3229–3237.
[10] R. Venkata Krishnan, K. Nagarajan, P.R. Vasudeva Rao, Heat capacity measurements on $BaThO_3$ and $BaCeO_3$, Journal of Nuclear Materials 299 (2001) 29–31.
[11] Synthetic sapphire $Al_2O_3$, Certificate of Reference Materials 720, 1970, NBS, U.S. Dept. of Commerce, Washington, DC 20234, UAS.
[12] Powder diffraction files (inorganic phases), Joint Committee on Powder Diffraction Data (JCPDS), International Centre for Diffraction Data, 1999, ICDD card number 41-1089.
[13] L. Desgranges, M. Marcet, Y. Pontillon, F. Porcher, J. Lamontagne, P. Matheron, X. lltis, G. Baldinozi, Solid State Phenomena 172–174 (2011) 624–629.
[14] H. Kleykamp, Solubility of selected fission products in $UO_2$ and (U, Pu) $O_2$, Journal of Nuclear Materials 206 (1993) 82–86.
[15] R.D. Shannon, Revised effective ionic radii and systematic studies of interatomic distances in halides and chalcogenides, Acta Crystallographica A32 (1976) 751–767.
[16] L.B. Pankratz, Thermodynamic properties of oxides, U.S. Bureau of Mines Bulletin 24 (1984) 102–103.
[17] J.K. Fink, Thermophysical properties of uranium dioxide, Journal of Nuclear Materials 279 (2000) 1–18.
[18] H. Inaba, K. Naito, M. Oguma, Heat capacity measurements of $U_{1-y}Gd_yO_2$ ($0.00 \le y \le 0.142$) from 310 to 1500 K, Journal of Nuclear Materials 149 (1987) 341–348.
[19] T. Matsui, Y. Arita, K. Naito, Heat capacity measurments of $U_{1-y}La_yO_2$ ($y$=0.044, 0.090, 0.142) from 300–1500 K, Journal of Radioanalytical and Nuclear Chemistry 143 (1) (1990) 149–156.
[20] T. Matsui, T. Kawase, K. Naito, Heat capacity and electrical conductivities of $(U_{1-y}Eu_y)O_2$ ($y$=0.044 and 0.090) from 300–1500 K, Journal of Nuclear Materials 186 (1992) 254–258.
[21] K.C. Mills, F.H. Ponsford, M.J. Richardson, Heat capacity and enthalpy of $UO_2$ and gadolinia doped $UO_2$, Thermochimica Acta 139 (1989) 107–120.
[22] Y. Arita, T. Matsui, S. Hamada, High temperature heat capacities of $(U_{0.91}M_{0.09})O_2$ (where M is Pr, Ce, Zr) from 290 to 1410 K, Thermochimica Acta 253 (1995) 1–9.
[23] Y. Arita, H. Hamada, T. Matsui, High temperature heat capacities and electrical conductivities of $UO_2$ doped with simulated fission products for 2–10 at% burnup, Thermochimica Acta 247 (1994) 225–236.
[24] H. Inaba, K. Naito, M. Oguma, H. Masuda, Heat capacity measurements of gadalonia doped (7.3 mol%) $UO_2$ from 310–1370 K, Journal of Nuclear Materials 137 (1986) 176–178.